

Coupling of Torsion and OH-Stretching in tert-Butyl Hydroperoxide and its radical analog,

QOOH

Rachel Huchmala*

Where does this
point? 

Department of Chemistry, University of Washington, Seattle, WA 98195, USA

E-mail: rmhuch@uw.edu

Introduction

Atmospheric oxidation of volatile organic compounds invariably leads to formation of organic peroxy radicals. Under low NO_x conditions, bimolecular reactions with HO_2 and autoxidation reactions of these peroxy radicals lead to formation of large quantities of hydroperoxides.^{1,2} These organic hydroperoxides are central to the formation of highly oxygenated organic molecules which are known to contribute to ~~particle~~ ^{What Particles?} formation and growth.^{3–6} Direct atmospheric spectroscopic observations of trace species like hydroperoxides are difficult and rely on accurate laboratory reference spectra.^{7,8} There have been a number of laboratory based measurements of vibrational spectra of hydroperoxides in the fundamental and overtone OH-stretching regions.^{9–16} In addition, recent spectroscopic studies of the OH-stretching regions of ~~TBHP~~ ^{abbr. not defined yet} have been conducted.^{17,18} From a theoretical perspective, analyses of spectra of hydroperoxides have previously been largely based on empirical models rather than *ab initio* calculations.^{12,14}

Interpretation of experimental vibrational spectra can be difficult, and both empirical and *ab initio* models are often needed to provide a coherent interpretation. Widely available approaches for solving the vibrational Schrödinger equation, such as generalized second-order vibrational perturbation theory (GVPT2), have been ^{not sure if I would use} ~~tremendously~~ successful for rigid and semi-rigid molecules of increasing dimension.^{19,20} However, for floppy molecules with ^{multiple minima} ~~more than one energy minimum~~ on the potential energy surface connected by small barriers, the local polynomial expansions of the potential energy surface used in most of these calculations are insufficient. Vibrational models specifically tailored to address the encountered difficulties are needed for these systems. Historically, empirical models with parameters either directly derived or ~~fitted~~ ^{fit?} based on different spectroscopic regions have been used to explain spectroscopic features that are otherwise inaccessible. For example, the empirical model developed by Likar *et al.* for ^{abbr. should be defined earlier} ~~tert-butyl hydroperoxide (TBHP)~~,¹² which is based on an adiabatic separation of the OH-stretch and the COOH torsion, was used to explain spectroscopic features in the OH-stretching overtone regions. With this model, Likar *et al.*

were able to quantify the height of the barrier that connects the two equivalent minima on the potential surface that describes the COOH torsion in TBHP, and its variation with the OH-stretching quantum number, v_{OH} . Similar empirical models have been successfully applied to other hydroperoxides such as hydrogen peroxide, methyl hydroperoxide, and ethyl hydroperoxide.^{10,14,15,21} The fact that a single empirical model can explain a range of spectroscopic features across a class of molecules gives confidence in the validity of the underlying assumptions of the model. [Nevertheless], the model ignores the contributions from the other degrees of freedom, as well as the coordinate dependence of the dipole moment function.

However, for hydroperoxides, there is evidence that the dependence of the dipole moment on the torsional angle needs to be included for more quantitative spectroscopic predictions.¹⁵

In general, a high-frequency OH-stretching motion and a low-frequency torsional motion may be modelled using an adiabatic separation. Including both of these motions explicitly in any model is imperative because this coupling leads to complicated spectra that, at room temperature, consist of multiple transitions from thermally excited torsional states. This is seen in studies of HOONO, where the stretch-torsion coupling significantly complicates the OH-stretching regions, and within each OH-stretching region multiple features of comparable intensity are observed.^{22,23} Using an adiabatic approximation, the OH-stretching regions of the IR spectra of TBHP and other similar molecules can be modeled effectively by considering only the effect of increasing quanta of OH excitation on the change in the torsional potential and shape of the dipole moment function.

This work focuses on a vibrational model built using the reaction path (RP) formalism.²⁴ This model provides coherent interpretation of the OH-stretching regions ($\Delta v_{\text{OH}} = 1 - 5$) of TBHP resulting in good agreement with both jet-cooled ($\Delta v_{\text{OH}} = 2$) and room temperature experimental spectra ($\Delta v_{\text{OH}} = 1 - 5$).^{17,18} The model includes one local mode (LM) OH-stretching coordinate, one torsional RP coordinate, and a harmonic treatment of the remaining 40 normal modes based on a quadratic expansion of the potential surface along the RP. In this analysis, it has been found that inclusion of the dipole moment function is

This analysis finds?
not sure about wording here

important to describe the relative intensity of the two major features observed within the OH-stretching regions for $\Delta v_{\text{OH}} \leq 3$, and show how the OH-stretching regions of TBHP are complicated by multiple transitions at room temperature. Finally, this work discusses how the RP model developed can be applied to the *tert*-butyl radical, QOOH .²⁵ With slight modifications, discussed in the text, the model shows promise for interpreting the OH-stretching regions of QOOH to the level of qualitative accuracy it has for TBHP.

Methods

Adiabatic Separation

The adiabatic separation of the COOH torsional mode from the other vibrational modes is the heart of this model. Similar to previous 2D models, we write the Hamiltonian for the OH-stretch and torsion as¹²

$$\hat{H}_{\text{tor},\text{OH}}\Psi(r,\tau) = \left[\frac{1}{2}p_\tau G_{\tau\tau}(r,\tau)p_\tau + \frac{p_r^2}{2\mu_{\text{OH}}} + V(r,\tau) \right] \Psi(r,\tau) \quad (1)$$

where r is the OH bond length, τ is the COOH torsional angle, $p_r = \frac{\hbar}{i}\frac{\partial}{\partial r}$, $p_\tau = \frac{\hbar}{i}\frac{\partial}{\partial \tau}$, μ_{OH} is the reduced mass for an OH group, $G_{\tau\tau}(r,\tau)$ is the coordinate-dependent Wilson G -matrix element for the torsion,^{26,27} and $V(r,\tau)$ is the potential energy surface. The ~~order of magnitude~~^{magnitude of the} difference between the OH-stretching and COOH torsion frequencies motivates the use of an adiabatic separation of these degrees of freedom, i.e., the wave functions are written as

$$\Psi(r,\tau) = \phi_{v_{\text{OH}}}(r;\tau)\chi_{n_{\text{tor}}}^{(v_{\text{OH}})}(\tau) \quad (2)$$

where the upper index on the torsional wave function specifies its dependence on the OH-stretching quantum number, v_{OH} . The number of quanta in the torsion is represented by n_{tor} . This product form is denoted by $|v_{\text{OH}}\rangle|n_{\text{tor}}\rangle$, while the $(r;\tau)$ notation indicates a parametric dependence on τ . The OH-stretching wave functions and energy levels for different torsional

angles are obtained by solving

$$\begin{aligned}\hat{H}_{\text{OH}}\phi_{\text{v}_{\text{OH}}}(r; \tau) &= \left[\frac{p_r^2}{2\mu_{\text{OH}}} + V(r, \tau) \right] \phi_{\text{v}_{\text{OH}}}(r; \tau) \\ &= V_{\text{v}_{\text{OH}}}^{\text{eff}}(\tau) \phi_{\text{v}_{\text{OH}}}(r; \tau)\end{aligned}\quad (3)$$

where $V_{\text{v}_{\text{OH}}}^{\text{eff}}(\tau)$ contains several contributions. The largest contribution is $E_{\text{v}_{\text{OH}}}(\tau)$, which is the vibrational energy in the OH-stretch for the $|\text{v}_{\text{OH}}\rangle$ state (determined by $V(0, \tau)$) that shows a weak, but significant, dependence on τ . The leading contribution to the torsion dependence of $V_{\text{v}_{\text{OH}}}^{\text{eff}}(\tau)$ comes from the τ -dependence of the electronic energy, $V(0, \tau)$. Inclusion of only $E_{\text{v}_{\text{OH}}}(\tau)$ and $V(0, \tau)$ in the definition of $V_{\text{v}_{\text{OH}}}^{\text{eff}}(\tau)$ leads to the approach that will be referred to as the 2D model in the discussion that follows, while the reaction path (RP) *already defined* model used in this study includes the harmonic zero-point energies for the other degrees of freedom in $V_{\text{v}_{\text{OH}}}^{\text{eff}}(\tau)$. All electronic structure calculations in this study were performed at the B2PLYP-D3/cc-pVTZ level of theory/basis as implemented in Gaussian16.²⁸ The τ -dependent effective torsional potentials, $V_{\text{v}_{\text{OH}}}^{\text{eff}}(\tau)$, provide a set of adiabatic potential curves consisting of one for each of the OH-stretching vibrational levels. The torsional energy levels and wave functions are obtained by solving

$$\begin{aligned}\langle \text{v}_{\text{OH}} | \hat{H}_{\text{tor}, \text{OH}} | \text{v}_{\text{OH}} \rangle | \text{n}_{\text{tor}} \rangle \\ = \left[\frac{1}{2} p_\tau \langle \text{v}_{\text{OH}} | G_{\tau\tau}(r, \tau) | \text{v}_{\text{OH}} \rangle p_\tau + V_{\text{v}_{\text{OH}}}^{\text{eff}}(\tau) \right] | \text{n}_{\text{tor}} \rangle \\ = E_{\text{v}_{\text{OH}}, \text{n}_{\text{tor}}} | \text{n}_{\text{tor}} \rangle\end{aligned}\quad (4)$$

where $E_{\text{v}_{\text{OH}}, \text{n}_{\text{tor}}}$ is the energy of the torsional state on a given effective potential, including the energy of the associated OH-stretching state.

Reaction Path (RP) Model

In the RP model, cuts through the potential and dipole surfaces were evaluated as functions of the COOH torsion angle, *while? in which?* where the other 41 internal coordinates were relaxed to minimize the electronic energy. The coordinates and energy were collected at each point in the scan, and a harmonic calculation was performed to obtain the gradient and Hessian at each geometry. In addition, one-dimensional OH-stretching cuts in the potential around each of these geometries were evaluated. For these cuts, the remaining 41 internal coordinates were constrained to the values obtained in the original torsion scan, *using*.

~~The remaining 41 vibrations were accounted for by~~ a RP analysis as described by Miller, Handy, and Adams.²⁴ This approach yields $3N-7$ normal modes and corresponding frequencies. Within this treatment, the excluded vibrational mode is defined by the normalized gradient vector in mass-weighted coordinates and describes the reaction coordinate at that geometry.²⁴ It should be noted that the vibration with the largest associated frequency is the OH-stretch, and this mode is removed from the remainder of the RP analysis. *Why?* After removing the COOH torsion and OH-stretch, the remaining 40 harmonic frequencies were summed and divided by two to obtain the harmonic zero-point energy of these vibrations ($V_{\text{ZPVE}}(\tau)$). This zero-point vibrational energy was added to the electronic energy ($V(0, \tau)$) leading to

$$V_{\text{v}_{\text{OH}}}^{\text{eff}}(\tau) = E_{\text{v}_{\text{OH}}}(\tau) + V(0, \tau) + V_{\text{ZPVE}}(\tau) \quad (5)$$

For each torsional angle, OH-stretching potentials were obtained by displacing the OH bond length from the equilibrium bond length ($r_e(\tau)$) by ~~-0.2 to 1.0 Å~~, in increments of 0.02 Å, at the given value of τ . The OH vibrational energies and wave functions were evaluated using one-dimensional discrete variable representations (DVR) as described by Colbert and Miller²⁹ to solve Eq. (3). A total of 2000 DVR points within the range of ~~-0.35 to 1.15 Å~~ were used, and a cubic spline was used to obtain the values of $V(r, \tau)$ at the desired geometries. The torsional wave functions were obtained by solving Eq. (4) in a particle on a ring (POR) basis,

where $G_{\tau\tau}(r, \tau)$ is the Wilson G -matrix element for the COOH torsion.²⁶ To facilitate this calculation, $V_{\text{v}_{\text{OH}}}^{\text{eff}}(\tau)$ and $\langle \text{v}_{\text{OH}} | G_{\tau\tau}(r, \tau) | \text{v}_{\text{OH}} \rangle$ were fit to expansions in $\cos(k\tau)$ with $k \leq 6$.

Determining Intensities

The transition dipole moments were calculated by first embedding the raw dipole moments in an Eckart frame with a reference structure where $\tau = 180^\circ$.^{30,31} In this study, this structure was chosen to capture the symmetry of the double-well potential along the torsion coordinate.^{32,33} The intensity (oscillator strength) of a transition ($|\text{v}_{\text{OH}}\rangle|n_{\text{tor}}\rangle \rightarrow |\text{v}'_{\text{OH}}\rangle|n'_{\text{tor}}\rangle$) is given by^{34,35}

$$f = 4.702 \cdot 10^{-7} [\text{cm} \cdot \text{D}^{-2}] \tilde{\nu}_{\text{v}_{\text{OH}}, n_{\text{tor}} \rightarrow \text{v}'_{\text{OH}}, n'_{\text{tor}}} \left| \langle n_{\text{tor}} | \vec{M}_{\text{v}_{\text{OH}} \rightarrow \text{v}'_{\text{OH}}}(\tau) | n'_{\text{tor}} \rangle \right|^2 \quad (6)$$

where

$$\vec{M}_{\text{v}_{\text{OH}} \rightarrow \text{v}'_{\text{OH}}}(\tau) = \langle \text{v}_{\text{OH}} | \vec{\mu}(r, \tau) | \text{v}'_{\text{OH}} \rangle \quad (7)$$

provides the transition dipole moment as a function of τ , $\vec{\mu}(r, \tau)$ is the dipole moment function, and $\tilde{\nu}_{\text{v}_{\text{OH}}, n_{\text{tor}} \rightarrow \text{v}'_{\text{OH}}, n'_{\text{tor}}}$ is the transition wavenumber. Within a Franck-Condon treatment, the components of $\vec{M}_{\text{v}_{\text{OH}} \rightarrow \text{v}'_{\text{OH}}}(\tau_e)$ depend only on the OH-stretching wave functions associated with the transition, and the intensity is given by

$$f_{\text{FC}} = 4.702 \cdot 10^{-7} [\text{cm} \cdot \text{D}^{-2}] \tilde{\nu}_{\text{v}_{\text{OH}}, n_{\text{tor}} \rightarrow \text{v}'_{\text{OH}}, n'_{\text{tor}}} \left| \vec{M}_{\text{v}_{\text{OH}} \rightarrow \text{v}'_{\text{OH}}}(\tau_e) \langle n_{\text{tor}} | n'_{\text{tor}} \rangle \right|^2 \quad (8)$$

Results and Discussion

For hydroperoxides, the torsional barrier connecting the minima on the potential energy surface, with torsion around the OO-bond (C-O-O-H dihedral), is comparable to the torsional frequency and the thermal energy at room temperature.^{10,12,14,15,21} As a result, multiple torsional states will be populated and the associated wave functions will be delocalized among these minima. The normal mode vibrational models that are implemented in quantum chemistry programs, are in general not expected to give an accurate representation of such delocalized vibrations. The TBHP torsion potential (Figure 1) is a symmetric double-well potential with a barrier at $\tau = 180^\circ$ of around 300 cm^{-1} , connecting two equivalent minima at $\tau = 113^\circ$ and 247° . The tunneling split torsional states are either symmetric (+) or asymmetric (-) around $\tau = 180^\circ$, and members of the pairs of torsional states (e.g. $|0_+\rangle$ and $|0_-\rangle$) have different energies. The tunneling splitting becomes larger with increasing excitation of the torsion, with the tunneling splitting of the torsional ground state pair being only a few cm^{-1} , while the pairs of torsional states above the barrier are significantly split.

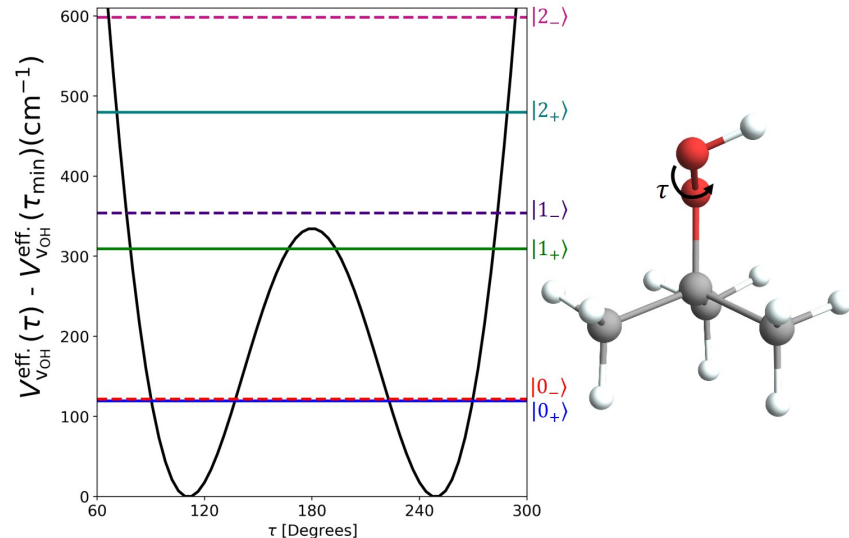


Figure 1: Effective potential as a function of the COOH torsion angle (τ) (right) and energy levels for the $v_{\text{OH}}=0$ state of TBHP (left).

The 2D Model

This analysis of the OH-stretching and torsional transitions begins with a 2D adiabatic Franck-Condon model that considers only the OH-stretch and the COOH torsion. By later relaxing these two approximations, that is, explicitly accounting for the dipole moment surface and including more degrees of freedom in the potential, we are able to determine the magnitude of the effect of each approximation and whether or not it should be used in modelling future systems. Results from this model are seen in Table 1, where they are compared to the experimental spectra of Vogt *et al.*¹⁸ The frequencies show a semi-constant blue shift from experiment. This shift is most likely due to ignoring the other vibrational degrees of freedom, but the choice of level of electronic structure theory could also have a role. The relative intensities, which are calculated using the Franck-Condon approach described by Equation 8 are denoted as RI_{FC}. This approach predicts an increasing relative intensity of the combination feature with increasing Δv_{OH} , in agreement with the experimental spectra and the results of the 2D empirical model used by Likar *et al.*¹² However, the relative intensity of the stretch-torsion combination feature is underestimated with the largest deviation of an order of magnitude found for the $\Delta v_{\text{OH}} = 1$ transitions.

Table 1: Experimental and calculated OH-stretching transition wavenumbers ($\tilde{\nu}$ in cm^{-1}) and relative intensities (RI in %) of the combination feature, compared to the OH-stretching feature. These are evaluated with the 2D model within the Franck-Condon approximation (RI_{FC}) and using the full dipole moment surface (RI_{DMS}).

Δv_{OH}	$\tilde{\nu}_{\text{OH}}^a$	$\tilde{\nu}_{\text{OH}}(\text{Expt.})^b$	RI _{FC} ^c	RI _{DMS} ^c	RI(Expt.) ^b
1	3615	3597	0.84	13.3	11.0 ± 2.8
2	7056	7017	4.05	9.96	13.3 ± 1.2
3	10323	10246	10.8	15.6	16.8 ± 1.3
4	13421	13307	21.2	24.3	47.4 ± 1.8
5	16356	16145	33.5	34.9	-

^a The calculated transition wavenumbers are for the $|0\rangle|0_+\rangle \rightarrow |v_{\text{OH}}\rangle|0_+\rangle$ transition.

^b From Vogt *et al.*¹⁸ The experimental transition wavenumbers are maxima of the OH-stretching features and RI is the ratio of the integrated intensities.

^c The ratio is calculated from summations over all transitions that contribute to the two features at $T = 300$ K.

The Torsion Dependent Transition Dipole Moment

To understand the origins of the underestimation of the relative intensities at low Δv_{OH} based on the Franck-Condon treatment (Equation 8), we next consider how the calculated relative intensities change when the full dipole surface is used in the calculations (Equation 6). As can be seen from the RI_{DMS} values reported in Table 1, the agreement between experiment and calculation is significantly improved compared with the RI_{FC} values.

Interestingly, while the use of the full transition dipole moment surface in the calculation of the intensities greatly increases the ratio of the intensities of the transitions of the combination feature to the OH-stretching feature for the $\Delta v_{\text{OH}} = 1$ region, the relative intensity for the $\Delta v_{\text{OH}} = 5$ region displays only a modest change. The questions naturally arise as to why the relative intensity for $\Delta v_{\text{OH}} = 1$ is most sensitive to the shape of the transition dipole surface and why this sensitivity decreases with OH-stretching excitation. To explore this, we focus on the four transitions between the states with $v_{\text{OH}} = 0$ and $n_{\text{tor}} = 0_{\pm}$ and the higher energy OH-stretching states with either $n_{\text{tor}} = 0_{\pm}$ or 1_{\pm} . These are the dominant transitions in the OH-stretching or combination feature, respectively, and the relative intensities are provided in Table 2. While the intensities of individual transitions differ, the sum of intensities of the transitions to the 0_{\pm} levels (OH-stretching feature) differ by less than 7% when calculated with or without the Franck-Condon approximation. The total intensity of the transitions to the 1_{\pm} levels (combination feature) show greater variation. The intensities of transitions that do not change the value of n_{tor} depend primarily on the overlap of the torsional wave functions for the two v_{OH} states, with the magnitude of the intensity determined by $|\langle 0 | \vec{\mu}(r, \tau_e) | v_{\text{OH}} \rangle|^2$ (see Equation 8). The transitions that change n_{tor} by one reflect both the overlaps, which are captured in the Franck-Condon treatment, and the slope of the transition dipole moment at τ_e that arise from the next term in the expansion of $\langle n_{\text{tor}} | \langle 0 | \vec{\mu}(r, \tau) | v_{\text{OH}} \rangle | n'_{\text{tor}} \rangle$ in Equation 6.

ratio of
intensities
to
Stretch
feature?

Table 2: Comparison of relative transition intensities for $\Delta v_{\text{OH}} = 1 - 5$, for the torsional transitions from $n_{\text{tor}} = 0 \pm$, using the Franck-Condon approximation (RI_{FC}) and using the full dipole moment surface (RI_{DMS}). n_{tor} and n'_{tor} denotes the initial and final torsional state, respectively.

Δv_{OH}		1		2		3		4		5	
n_{tor}	n'_{tor}	RI_{DMS}	RI_{FC}								
0 ₊	0 ₊	1.00	1.81	1.00	1.56	1.00	1.33	1.00	1.17	1.00	1.11
0 ₊	0 ₋	0.81	0.00	0.47	0.00	0.27	0.00	0.13	0.00	0.08	0.00
0 ₋	0 ₊	0.81	0.00	0.47	0.00	0.28	0.00	0.14	0.00	0.08	0.00
0 ₋	0 ₋	0.96	1.80	0.99	1.56	1.00	1.34	1.01	1.18	1.02	1.12
Sum		3.58	3.61	2.93	3.12	2.55	2.67	2.28	2.35	2.17	2.23
0 ₊	1 ₊	0.19	0.01	0.11	0.05	0.14	0.11	0.18	0.17	0.23	0.23
0 ₊	1 ₋	0.00	0.00	0.00	0.00	0.00	0.00	0.00	0.00	0.01	0.00
0 ₋	1 ₊	0.00	0.00	0.00	0.00	0.00	0.00	0.00	0.00	0.01	0.00
0 ₋	1 ₋	0.17	0.01	0.09	0.04	0.12	0.08	0.16	0.14	0.21	0.21
Sum		0.36	0.02	0.2	0.09	0.26	0.19	0.35	0.31	0.46	0.44

In Figure 2, the torsion-dependent transition dipole moments for the $\Delta v_{\text{OH}} = 1$ and $\Delta v_{\text{OH}} = 5$ transitions are shown. Based on the symmetry of the components of the transition dipole moment, transitions between states of the same symmetry will be A/B-type, whereas transitions between states of different symmetry will be C-type.

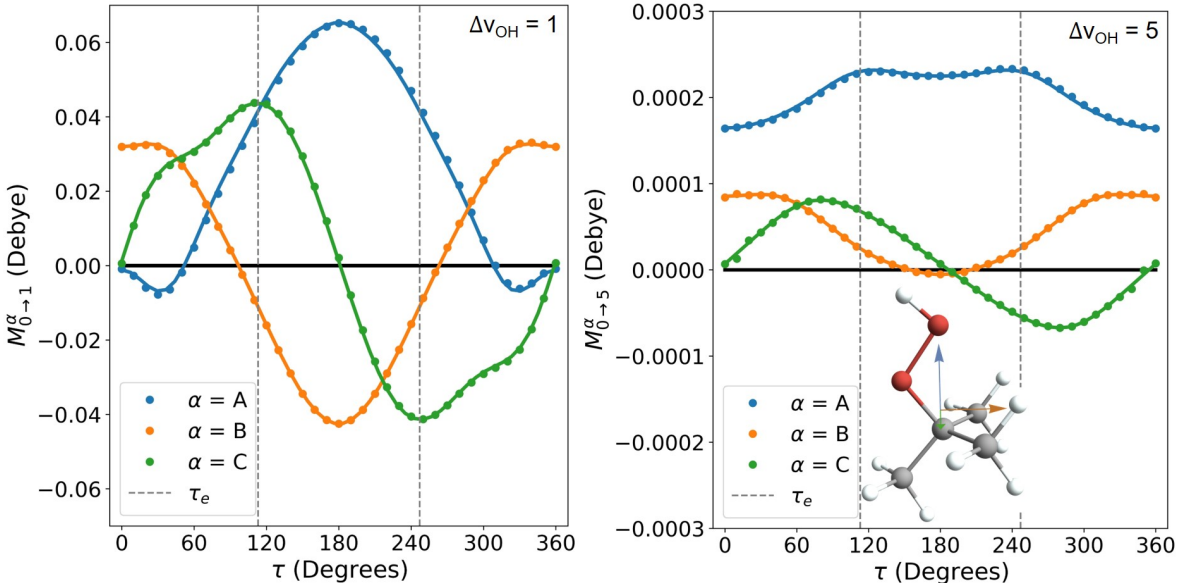


Figure 2: Components of the OH-stretching transition dipole moment, $\vec{M}_{v_{\text{OH}} \rightarrow v'_{\text{OH}}}(\tau)$ in Equation 7 are plotted as functions of the torsional angle for $\Delta v_{\text{OH}} = 1$ (left) and 5 (right). The inset in the right panel shows the principal axis system.

The relative contribution of the Franck-Condon term and the next term in the expansion of the transition dipole moment depends on the ratio of the slope of the transition dipole moment to its value. This ratio near τ_e (dashed vertical line, Figure 2) is larger for the $\Delta v_{\text{OH}} = 1$ than $\Delta v_{\text{OH}} = 5$ transition for the A-component, which dominates the intensity of the combination feature, as seen in Table 3. This table shows the calculated ratio of the slope of the components of the transition dipole moments,

$$M_{v_{\text{OH}} \rightarrow v'_{\text{OH}}}^{\alpha}(\tau) = \langle v_{\text{OH}} | \mu_{\alpha}(r, \tau) | v'_{\text{OH}} \rangle \quad (9)$$

to the value of $M_{v_{\text{OH}} \rightarrow v'_{\text{OH}}}^{\alpha}(\tau_e)$,

$$R_{v_{\text{OH}} \rightarrow v'_{\text{OH}}}^{\alpha}(\tau_e) = M_{v_{\text{OH}} \rightarrow v'_{\text{OH}}}^{\alpha'}(\tau_e) / M_{v_{\text{OH}} \rightarrow v'_{\text{OH}}}^{\alpha}(\tau_e) \quad (10)$$

Here, the α superscript represents the A , B , or C component of $\vec{M}_{v_{\text{OH}} \rightarrow v'_{\text{OH}}}(\tau_e)$

Table 3: Values of the A, B and C components of $R_{v_{\text{OH}} \rightarrow v'_{\text{OH}}}^{\alpha}(\tau_e)$ based on Eq (10), for $\Delta v_{\text{OH}} = 1 - 5$

Δv_{OH}	1	2	3	4	5
A	0.9351	-0.6456	0.2434	0.1729	0.0933
B	4.3118	5.3895	-33.1633	-4.4397	-1.9523
C	0.0543	-0.3871	-0.4987	-0.5374	-0.5133

The RP Model

The above discussion outlines the effect of the full transition dipole moment and how it's inclusion results in consistent relative intensities with experiment. But, the 2D treatment of the potential still has a blue shift in frequency. This shift is most likely due to the omission of 40 of the vibrational modes by the 2D model, as well as possible deficiencies in the DFT level of theory. The RP model looks to account for the first of these by incorporating the harmonic zero point vibrational energy (ZPVE) into the electronic potential to account for some of this deviation. Results of this calculation can be found in Table 4.

Table 4: Calculated torsional barrier heights (V_τ in cm^{-1}), calculated and experimental OH-stretching transition wavenumbers ($\tilde{\nu}_{\text{OH}}$ in cm^{-1}) and relative intensities (RI in %) of the combination feature compared to the OH-stretching feature.

$\Delta\nu_{\text{OH}}$	V_τ ^a	$\tilde{\nu}_{\text{OH}}$ ^b	$\tilde{\nu}_{\text{OH}}(\text{Expt.})$ ^c	RI_{DMS} ^d	$\text{RI}(\text{Expt.})$ ^c
1	377	3615	3597	13.7	11.0 ± 2.8
2	432	7055	7017	9.92	13.3 ± 1.2
3	505	10322	10246	15.5	16.8 ± 1.3
4	595	13419	13307	24.0	47.4 ± 1.8
5	600	16354	16145	34.3	-

^a The ground state barrier calculated is 335 cm^{-1}

^b The calculated transition wavenumbers are for the $|0\rangle|0_+\rangle \rightarrow |\text{v}_\text{OH}\rangle|0_+\rangle$ transition.

^c From Vogt *et al.*¹⁸ The experimental transition wavenumbers are maxima of the OH-stretching features and RI is the ratio of the integrated intensities.

^d The ratio is calculated from summations over all transitions that contribute to the two features at $T = 300 \text{ K}$.

While the differences in both OH-stretching transition frequency and relative intensity are subtle, valuable information can still be obtained from this RP model. First, the results of this model are in good qualitative agreement with experimental findings as seen in Figure 3. The simulated spectra were obtained using PGOPHER and Boltzmann weighted torsional states.³⁶ Albeit shifted, the features of the spectra are comparable in intensity and structure.

is there a
second... ?

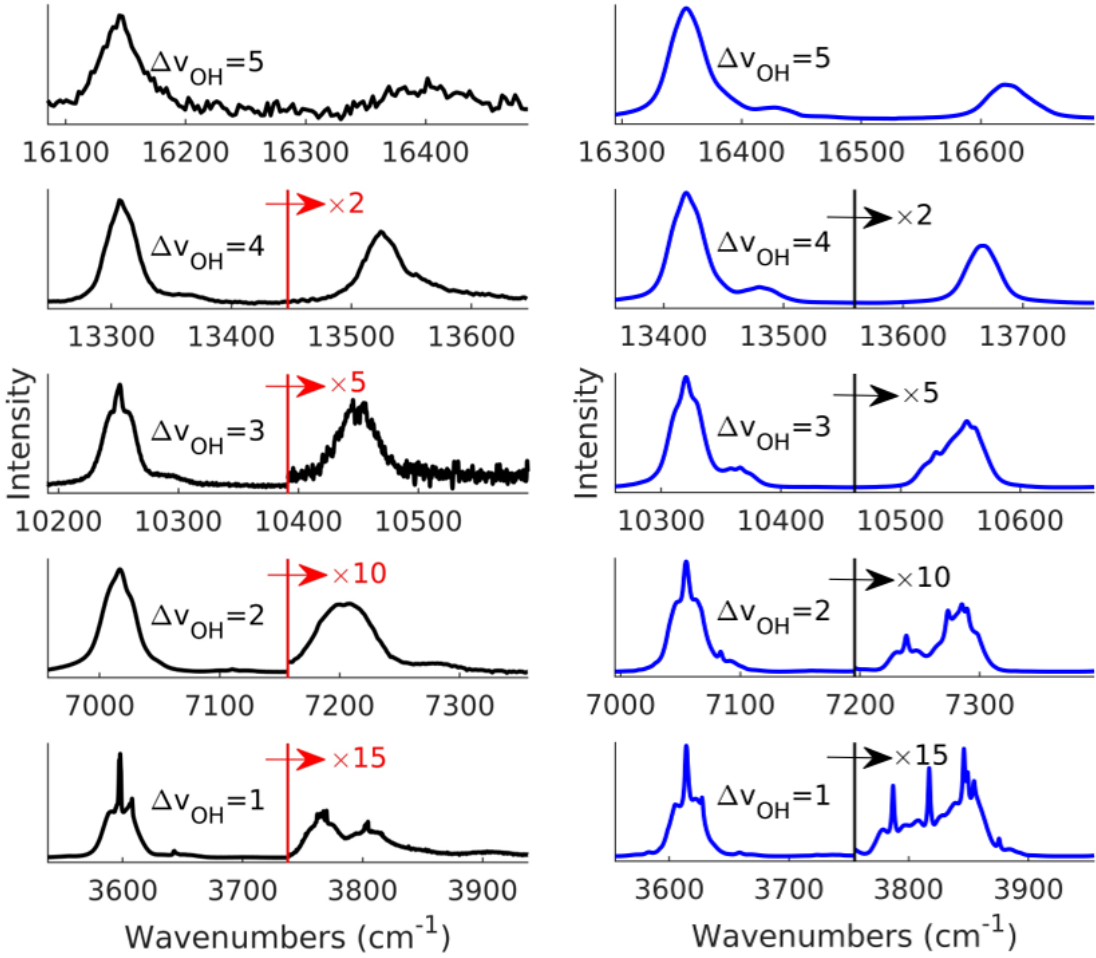


Figure 3: Left: Experimental room temperature ($T = 300$ K) spectra collected by Vogt *et al.*¹⁸ Right: Calculated room temperature ($T = 300$ K) spectra of the $\Delta v_{\text{OH}} = 1 - 5$ regions of TBHP based on the parameters obtained from the RP model. In both, the maxima of the OH-stretching features (left features) have been aligned and the wavenumber range is equivalent for all spectra. The portions of the spectra to the right of the red (left) and black (right) lines have been multiplied by the factors given in the figure to show the structure of the OH-stretch torsion combination feature.

With further investigation we can uncover the reasons for the blue shift seen in the frequencies. First, by using a higher-level of theory in the electronic structure calculations, CCSD(T)-F12(a)/cc-pVDZ-F12, we saw the barrier of the electronic torsional potential decrease by ~ 49 cm^{-1} . This results in a decrease of the transition wavenumbers throughout the OH-stretching regions.¹⁸ Furthermore, the reaction path results can be used to deter-

mine which other modes are perturbing the OH-stretch and COOH torsion. In Figure 4, the changes in the harmonic zero point vibrational energy (Δ ZPVE) for selected local modes as functions of the OH bond length (left panel) and torsion angle (right panel), over the ranges sampled by the wave functions for the states of interest. From this data is it seen that Δ ZPVE for the OOH-bend changes significantly as the OH bond length is extended, a change of ~ 150 cm $^{-1}$ at the maximum which implies that the frequency of the OOH-bend changes significantly as the OH bond length is extended and therefore coupled to the OH-stretching and COOH torsion modes.

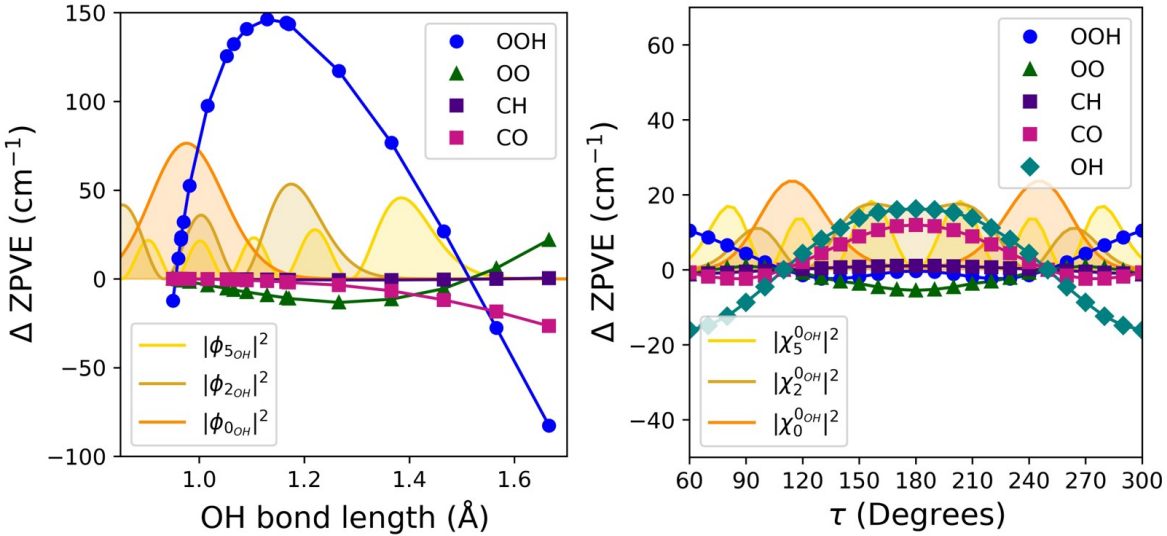


Figure 4: Variation of local mode harmonic frequencies plotted as functions of the OH-stretching bond length (left) and torsional angle (right). Probability amplitudes for $v_{OH} = 0$, 2 and 5 at τ_e are shown for the OH-stretch (left), and for $n_{tor} = 0_+, 1_+$ and 2_+ torsion states when $v_{OH} = 0$ (right).

Conclusions

Through this work we have created a straight-forward model to semi-quantitatively reproduce experimental vibrational spectra of the OH-stretching regions of TBHP. We have determined that it is necessary to include the torsional dependence of the dipole moment to accurately describe the combination band of OH-stretch+ n_{tor} . Also notable from the dipole moment study, with respect to the OH-stretching intensity itself, in the Franck-Condon treatment there is a redistribution of the intensity such that either treatment produces a similar sum of relative intensity (Table 2). In order to address the blue shift of the data, a RP model is employed. Although it does not change the values much, it provides valuable insight into other modes of TBHP that are coupling with these motions. As with the 2D model, the resulting simulated spectra of the RP model are in good qualitative agreement with experimental findings.

Future Work

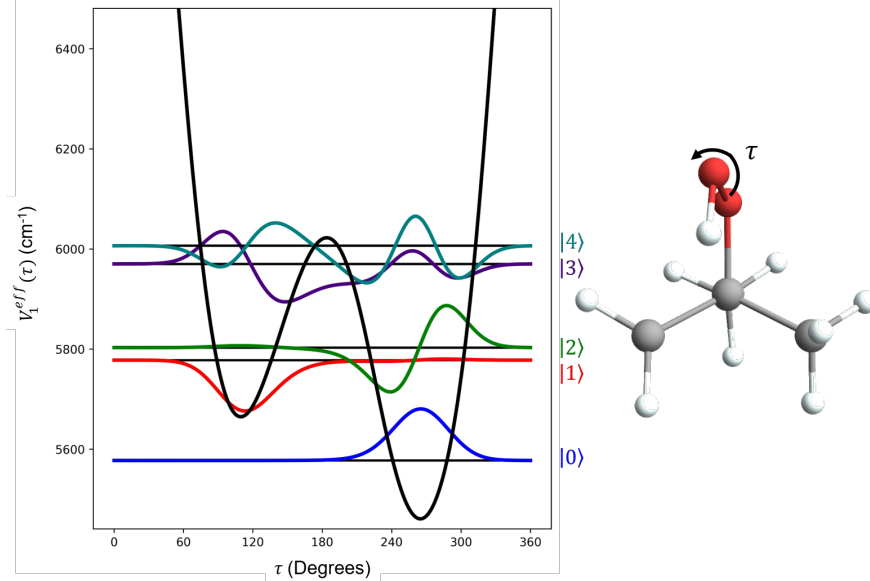


Figure 5: Effective potential as a function of the COOH torsion angle (τ) (right) and energy levels for the $v_{\text{OH}}=0$ state of QOOH (left).

Extensions to Radical Products

The previously described model includes an approximation for a system with a torsional potential that is symmetric about 180° , like TBHP or other hydroxides. When investigating radical products like QOOH (Figure 5), the symmetry of the double well about 180° is broken. Therefore, small adjustments need to be made to the treatment of the torsional potentials ($V_{\text{VOH}}^{\text{eff}}(\tau)$). The torsional potentials are fit to Fourier expansions of $\cos(k\tau) + \sin(m\tau)$, but when symmetric about 180° , the sine terms in the expansion can be ignored. Therefore, we use expansions in $\cos(k\tau)$ with $k \leq 6$ and a POR basis for the TBHP study. Since QOOH is asymmetric about 180° , both the cosine and sin terms of the expansion are necessary. This leads to the POR representation having a complex Hamiltonian and returning complex wave functions, requiring adjustments to all prior equations. To circumvent this, we will use an expansion of $\cos(k\tau) + \sin(m\tau)$ with $k \leq 6$ and $m \leq 5$ and solve the Schrödinger equation using the 1D DVR on the range of 0 to 2π as described by Colbert and Miller.²⁹

For these calculations, a total of 201 DVR points from the Fourier fitted $V_{\text{VOH}}^{\text{eff}}(\tau)$ and the Wilson G-matrix element for the COOH torsion are used.²⁶ Now, with the torsional wave functions in hand, the intensities and other analysis will continue as previously described.

Next Steps

Future Directions of this project include conducting similar analysis of the OH-stretching regions in QOOH to provide context for experimental findings. By applying the insights we gained from TBHP, we hope to build a basis of understanding for the complexities of the QOOH vibrational spectrum. Not only will we address the COOH torsion, we are also planning to investigate the effect of the CH₂ rotation on the OH-stretching regions.

References

- (1) Hanst, P. L.; Gay, B. W. *Atmos. Environ.* (1967) **1983**, *17*, 2259–2265.
- (2) Crounse, J. D.; Nielsen, L. B.; Jørgensen, S.; Kjaergaard, H. G.; Wennberg, P. O. *J. Phys. Chem. Lett.* **2013**, *4*, 3513–3520.
- (3) Bonn, B.; von Kuhlmann, R.; Lawrence, M. G. *Geophys. Res. Lett.* **2004**, *31*.
- (4) Docherty, K. S.; Wu, W.; Lim, Y. B.; Ziemann, P. J. *Environ. Sci. Technol.* **2005**, *39*, 4049–4059.
- (5) Bianchi, F.; Kurtén, T.; Riva, M.; Mohr, C.; Rissanen, M. P.; Roldin, P.; Berndt, T.; Crounse, J. D.; Wennberg, P. O.; Mentel, T. F. et al. *Chem. Rev.* **2019**, *119*, 3472–3509.
- (6) Praske, E.; Otkjær, R. V.; Crounse, J. D.; Hethcox, J. C.; Stoltz, B. M.; Kjaergaard, H. G.; Wennberg, P. O. *Proc. Natl. Acad. Sci.* **2018**, *115*, 64–69.
- (7) Fu, D.; Millet, D. B.; Wells, K. C.; Payne, V. H.; Yu, s.; Guenther, A.; Eldering, A. *Nat. Commun.* **2019**, *10*, 1–12.
- (8) Brown, S. S. *Chem. Rev.* **2003**, *103*, 5219–5238.
- (9) Fry, J. L.; Matthews, J.; Lane, J. R.; Roehl, C. M.; Sinha, A.; Kjaergaard, H. G.; Wennberg, P. O. *J. Phys. Chem. A* **2006**, *110*, 7072–7079.
- (10) Closser, K. D.; Vogelhuber, K. M.; Hsieh, S. *J. Phys. Chem. A* **2008**, *112*, 1238–1244.
- (11) Chandler, D. W.; Farneth, W. E.; Zare, R. N. *J. Chem. Phys.* **1982**, *77*, 4447–4458.
- (12) Likar, M. D.; Baggott, J. E.; Crim, F. F. *J. Chem. Phys.* **1989**, *90*, 6266–6274.
- (13) Ticich, T. M.; Likar, M. D.; Dübal, H.; Butler, L. J.; Crim, F. F. *J. Chem. Phys.* **1987**, *87*, 5820–5829.

- (14) Homitsky, S. C.; Dragulin, S. M.; Haynes, L. M.; Hsieh, S. *J. Phys. Chem. A* **2004**, *108*, 9492–9499.
- (15) Matthews, J.; Martínez-Avilés, M.; Francisco, J. S.; Sinha, A. *J. Chem. Phys.* **2008**, *129*, 074316.
- (16) Chuang, M.-C.; Baggott, J. E.; Chandler, D. W.; Farneth, W. E.; Zare, R. N. *Faraday Discuss. Chem. Soc.* **1983**, *75*, 301–313.
- (17) Hansen, A. S.; Huchmala, R. M.; Vogt, E.; Boyer, M. A.; Bhagde, T.; Vansco, M. F.; Jensen, C. V.; Kjaersgaard, A.; Kjaergaard, H. G.; McCoy, A. B. et al. *J. Chem. Phys.* Accepted.
- (18) Vogt, E.; Huchmala, R. M.; Jensen, C. V.; Boyer, M. A.; Wallberg, J.; Hansen, A. S.; Kjaersgaard, A.; Lester, M. I.; McCoy, A. B.; Kjaergaard, H. G. *J. Chem. Phys.* Accepted.
- (19) Barone, V. *J. Chem. Phys.* **2005**, *122*, 014108.
- (20) Barone, V.; Biczysko, M.; Bloino, J. *Phys. Chem. Chem. Phys.* **2014**, *16*, 1759–1787.
- (21) Dübal, H. R.; Crim, F. F. *J. Chem. Phys.* **1985**, *83*, 3863–3872.
- (22) Schofield, D. P.; Kjaergaard, H. G.; Matthews, J.; Sinha, A. *J. Chem. Phys.* **2005**, *123*, 134318.
- (23) McCoy, A. B.; Sprague, M. K.; Okumura, M. *J. Phys. Chem. A* **2010**, *114*, 1324–1333.
- (24) Miller, W. H.; Handy, N. C.; Adams, J. E. *J. Chem. Phys.* **1980**, *72*, 99–112.
- (25) Moore III, K. B.; Turney, J. M.; Schaefer III, H. F. *J. Chem. Phys.* **2017**, *146*, 194304.
- (26) Wilson, E. B.; Decius, J. C.; Cross, P. C. McGraw-Hill: New York, 1955.
- (27) Frederick, J. H.; Woywod, C. *J. Chem. Phys.* **1999**, *111*, 7255–7271.

- (28) Frisch, M. J.; Trucks, G. W.; Schlegel, H. B.; Scuseria, G. E.; Robb, M. A.; Cheeseman, J. R.; Scalmani, G.; Barone, V.; Petersson, G. A.; Nakatsuji, H. et al. Gaussian[®]16 Revision C.01. 2016; Gaussian Inc. Wallingford CT.
- (29) Colbert, D. T.; Miller, W. H. *J. Chem. Phys.* **1992**, *96*, 1982–1991.
- (30) Eckart, C. *Phys. Rev.* **1935**, *47*, 552–558.
- (31) Krasnoshchekov, S. V.; Isayeva, E. V.; Stepanov, N. F. *J. Chem. Phys.* **2014**, *140*, 154104.
- (32) Pickett, H. M. *J. Chem. Phys.* **1972**, *56*, 1715–1723.
- (33) Lauvergnat, D.; Luis, J. M.; Kirtman, B.; Reis, H.; Nauts, A. *J. Chem. Phys.* **2016**, *144*, 084116.
- (34) Kjaergaard, H. G.; Yu, H.; Schattka, B. J.; Henry, B. R.; Tarr, A. W. *J. Chem. Phys.* **1990**, *93*, 6239–6248.
- (35) Atkins, P. W.; Friedman, R. S. Oxford university press, 2011.
- (36) Western, C. M. *J. Quant. Spectrosc. Radiat. Transf.* **2017**, *186*, 221–242.